Ability of multiangle remote sensing observations to identify and distinguish mineral dust types: Optical models and retrievals of optically thick plumes

O. V. Kalashnikova,[1] R. Kahn,[2] I. N. Sokolik,[3] and Wen-Hao Li[2]

Received 16 January 2004; revised 10 May 2004; accepted 14 July 2004; published 25 March 2005.

[1] We present a systematic theoretical study of atmospheric mineral dust radiative properties, focusing on implications for multiangle and multispectral remote sensing. We model optical properties of complex, nonspherical mineral dust mixtures in three visible-near-infrared satellite channels: 0.550, 0.672, and 0.866 μm, accounting for recent field and laboratory data on mineral dust morphology and mineralogy. To model the optical properties of mineral dust, we employ the discrete dipole approximation technique for particles up to 2 μm diameter and the T matrix method for particles up to 12 μm. We investigate the impact of particle irregularity, composition, and size distribution on particle optical properties, and we develop optical models for representative natural mineral dust composition-size-shape types. Sensitivity studies with these models indicate that Multiangle Imaging Spectroradiometer (MISR) data should be able to distinguish plate-like from grain-like dust particles, weakly from strongly absorbing compositional types, and monomodal from bimodal size distributions. Models containing grain-like, weakly absorbing, bimodal distributions of dust particles were favored for optically thick Saharan and Asian dust plume examples, whereas strongly absorbing and plate-like particles were rejected. We will present detailed, systematic MISR sensitivity studies and analysis of more complex field cases using the optical models derived here in a future paper.

Citation: Kalashnikova, O. V., R. Kahn, I. N. Sokolik, and W.-H. Li (2005), Ability of multiangle remote sensing observations to identify and distinguish mineral dust types: Optical models and retrievals of optically thick plumes, *J. Geophys. Res.*, *110*, D18S14, doi:10.1029/2004JD004550.

1. Introduction

[2] The quality of remote sensing aerosol optical depth retrievals depends critically upon the accuracy of particle optical property models assumed in the algorithms. Mineral dust nonsphericity, complex composition, and large spatial and temporal variability are important characteristics that complicate such retrievals. Recent research shows that mineral dust particle nonsphericity can have a profound effect on reflected intensity, and must be explicitly accounted for in aerosol retrievals [*Mishchenko et al.*, 1995; *Kalashnikova and Sokolik*, 2002]. So models that take into account dust particle nonspherical shapes and wavelength-dependent compositions might significantly improve our ability to retrieve aerosol optical depth, along with dust optical properties, globally, via satellites. Multiangle, multispectral instruments such as the Multiangle Imaging Spectroradiometer (MISR) [*Diner et al.*, 1999] and the Polarization and Directionality of Earth Reflectances (POLDER) [*Deuze et al.*, 2000] offer additional constrains that can be used to distinguish particle shapes [*Kahn et al.*, 1997]. These instruments may make it possible to account for nonspherical particles in satellite retrieval algorithm [*Mishchenko et al.*, 2003]. Recent field and laboratory work [*Clarke et al.*, 2004; *Huebert et al.*, 2000; *Okada et al.*, 2001; *Reid et al.*, 2003a, 2003b; *Wang et al.*, 2002] provide new information about the physical properties of mineral dust originating in various regions. Using published mineral dust physical properties as a guide, we systematically study how particle shape, size distribution, and composition affect the particle optical properties that multiangle instruments can distinguish. In section 2 we discuss the choice of representative shapes, compositions, and size distributions used for our dust optical models. Section 3 describes the modeling approach and then explores the effects of particle composition, shape, and size (CSS) on dust optical properties at three wavelengths (0.550, 0.672, and 0.866 μm). From these results, in section 4 we identify representative composition-shape-size distributions that we expect MISR to be able to distinguish. In section 5 we use the representative models in MISR retrieval algorithms to calculate dust reflectances and to compare these to MISR-measured reflectances for optically thick Saharan and Asian dust plume examples. We summarize our findings in section 6. We will provide

[1]National Research Council, Jet Propulsion Laboratory, Pasadena, California, USA.
[2]Jet Propulsion Laboratory, Pasadena, California, USA.
[3]School of Earth and Atmospheric Sciences, Georgia Institute of Technology, Atlanta, Georgia, USA.

0148-0227/05/2004JD004550$09.00

systematic case-by-case sensitivity studies for MISR, based on these particle optical models and will present retrieval validation studies using coincident MISR and fields observations for Saharan and Asian dust types in a future paper.

2. Dust Physical and Optical Properties Considered in This Study

[3] Heterogeneous atmospheric dust particles pose tremendous challenges to the radiative transfer models used in satellite retrieval algorithms because, unlike other aerosol types, airborne mineral dust particles exist as a mixtures of particles having radically different morphological and optical properties [*Sokolik et al.*, 2001]. Moreover, dust particle chemistry and morphology are wavelength-dependent [*Sokolik and Toon*, 1999], change during transport [*Maring et al.*, 2003], and vary over time even at fixed locations [*Anderson et al.*, 1992]. *Kalashnikova and Sokolik* [2004] modeled the optical properties of individual dust particle shapes and compositional types as well as several dust CSS distributions based on morphology and composition data for dust particles collected in the atmosphere at different locations during the last decade [*Parungo et al.*, 1995; *Choi et al.*, 2001; *Falkovich et al.*, 2001; *Ganor and Levin*, 1998; *Gao and Anderson*, 2001; *Huebert et al.*, 2000; *Koren et al.*, 2001; *Okada et al.*, 2001]. Here we extend this work, adding information from two recent field studies, the Puerto Rico Dust Experiment (PRIDE [*Reid et al.*, 2003b]) and the Aerosol Characterization Experiment in Asia (ACE-Asia [*Clarke et al.*, 2004]) that provide dust size and morphology data sets based on cross-correlated aerodynamic, optical and geometrical techniques. In addition, a new online data set giving experimentally measured scattering matrices for different minerals, including feldspar and clay minerals, has become available at http://www.astro.uva.nl/scatter/ [*Volten et al.*, 2005]. We use these data for comparison with the scattering phase functions of several dust types modeled in this study.

[4] We consider the following dust physical properties from previous modeling work [*Kalashnikova and Sokolik*, 2004] and from new PRIDE and ACE-Asia experiments:

[5] 1. Particle refractive index changes with wavelength and has to be modeled for each wavelength of interest [*Sokolik and Toon*, 1999].

[6] 2. Particle irregularity increases with size [*Huebert et al.*, 2000; *Okada et al.*, 2001; *Reid et al.*, 2003a; *Anderson*, 2003]. In these studies, particle irregularity is reported as a parameter that characterizes the circularity (CIR) of a particle's two-dimensional (2-D) projection:

$$\mathrm{CIR} = \mathrm{Perimeter}^2/(4\pi * \mathrm{Area}) \quad (1)$$

[7] 3. For mineral dust aerosols, there is no clear relationship between the measured 2-D aspect ratio and particle size, or between the 2-D aspect ratio and circularity [*Gao and Anderson*, 2001; *Okada et al.*, 2001; *Anderson*, 2003; *Reid et al.*, 2003a]. The mean value of the aspect ratio can vary from ~1.4 [*Okada et al.*, 2001] to 1.5–1.9 [*Gao and Anderson*, 2001] depending on dust source. Recent PRIDE measurements report an average value of 1.9 with a standard deviation of 0.9 [*Reid et al.*, 2003a].

[8] 4. Collection techniques for aerosols larger than 3 μm [*Clarke et al.*, 2004; *Reid et al.*, 2003b, 2003a] have recently improved, allowing us to model airborne dust particles having diameters in the range 0.1 to 12 μm.

[9] 5. Dust number size distributions in the range 0.1–12 μm, retrieved from optical counter measurements during ACE-Asia, require two lognormal modes to fit all conditions [*Clarke et al.*, 2004]. Dust volume size distributions measured by optical counters during PRIDE show a steep falloff below ~1 μm and a more gradual increase to a maximum near 10 μm [*Reid et al.*, 2003b], also suggesting a bimodal particle distribution. Dust samples from the Tajikistan desert are best fit with bimodal number distributions as well [*Sviridenkov et al.*, 1993].

[10] 6. The smaller-sized of the two dust modes measured during ACE-Asia appeared stable, insensitive to changing dust concentration, whereas the larger-sized mode was more variable, showing strong dependence on dust layer elevation, dust concentration, and dust source [*Clarke et al.*, 2004].

[11] 7. The dust number size distribution retrieved from individual particle analysis (IPA) during PRIDE appears monomodal, with 90% of the particles smaller than 3 μm in diameter [*Reid et al.*, 2003b].

[12] 8. During atmospheric transport, the fraction of larger-sized particles diminishes [*Maring et al.*, 2003; *Prospero*, 1999].

[13] 9. There are insufficient data to correlate particle composition and size in general. However, some IPA data from PRIDE show that small-sized dust particles are predominantly individual clays, and large-sized dust particles are clays internally aggregated with nonabsorbing quartz or sea salt [*Reid et al.*, 2003a]. Therefore the imaginary part of the refractive index of a particle is likely to decrease with size.

[14] 10. Circularity (equation (1)) considers only a two-dimensional projection of particle shape. The third dimension, particle depth (h), is usually combined with particle width (b) to give particle thickness (h/b). *Okada et al.* [2001] find the majority of Asian dust particles under 5 μm diameter are thin, plate-like, particles having $h/b \sim 0.3$. PRIDE data indicate that Saharan dust particles larger that 1 μm in diameter often exist in aggregated forms consisting primarily of grain-like silicates [*Reid et al.*, 2003a].

[15] On the basis of these observations and the constraints discussed below, we chose several representative size distributions, compositions and shapes to use in our retrieval models.

2.1. Particle Composition

[16] Iron oxide (hematite) strongly absorbs in the visible and practically determines particle absorption at visible and NIR wavelengths. To cover the expected range of mineral dust absorption, we adopt wavelength-dependent mineral dust refractive indices calculated for two limiting clay-hematite mineral aggregates [*Sokolik and Toon*, 1999]: composition type 1 (weakly absorbing), containing 1% hematite, and composition type 2 (strongly absorbing),

Table 1. Refractive Indices Representing Two Extremes of Mineral Dust Absorption

Wavelength, μm	Type 1	Type 2
0.550 (green)	(1.51, 0.0021)	(1.61, 0.0213)
0.672 (red)	(1.51, 0.0011)	(1.60, 0.0064)
0.866 (near-IR)	(1.51, 0.0007)	(1.59, 0.0032)

containing 10% hematite. Effective refractive indices for composition types 1 and 2 aggregates are presented in Table 1.

2.2. Particle Size Distribution

[17] In addition to the two size modes described by *Clarke et al.* [2004], dust samples collected at the source during major dust events can contain particles having diameters up to 100 μm. However, particles with diameters greater than 10–12 μm remain localized near the source, and are poorly characterized by most measurement techniques [*Clarke et al.*, 2004]. So we focus on particles having diameters <10 μm that dominate the transported dust plumes and most commonly observed by satellites [*Prospero*, 1999; *Gomes et al.*, 1990]. In light of the results summarized above, we adopt the following bimodal functional form to describe dust particle sizes:

$$\frac{dN}{d\log D_p} = \sum_{i=1}^{2} \frac{N_i}{\sqrt{2\pi}\log\sigma_i} \exp\left(-\frac{(\log D_p - \log D_{pi})^2}{2\log^2\sigma_i}\right) \quad (2)$$

where N is a number distribution, D_p is the geometric diameter, D_pi is the geometric mean diameter, and σ_i is the geometric standard deviation [*Clarke et al.*, 2004].

[18] On the basis of size distribution parameters measured during ACE-Asia and PRIDE, nominal parameter values in these distributions are D_{p1} = 1.0 μm and σ_1 = 1.5 for the smaller-sized mode (size mode 1) and D_{p2} = 2.0 μm and σ_2 = 2.0 for the larger one (size mode 2). The relative number concentration of size modes 1 and 2 is likely to change depending on dust source, wind conditions, and distance from the source region [*Clarke et al.*, 2004]. In addition, inconsistencies exist in size distributions measured by optical, aerodynamical and microscopy methods. These inconsistencies are extensively discussed by *Reid et al.* [2003b].

[19] To address uncertainties in the measured dust size distribution values and to account for spatial and temporal variations in the dust size distribution, we vary the geometrical mean diameter and the standard deviation of size modes 1 and 2 and then consider several dust mixing scenarios. We define these scenarios in terms of number concentration using the following percentages: (1) scenario A, 30% size mode 1 + 70% size mode 2; (2) scenario B, 50% size mode 1 + 50% size mode 2; and (3) scenario C, 80% size mode 1 + 20% size mode 2. PRIDE IPA data suggested the possibility of having 100% of mode 1 [*Reid et al.*, 2003a], so we also consider cases containing 100% of each mode.

2.3. Particle Shape

[20] Most readily available data on dust morphology and mineralogy come from individual particle analysis [*Choi et al.*, 2001; *Falkovich et al.*, 2001; *Ganor and Levin*, 1998; *Gao and Anderson*, 2001; *Koren et al.*, 2001; *Parungo et al.*, 1995; *Reid et al.*, 2003a], performed with electron microscopes [*McLaren*, 1991]. Despite the difficulty in observing all dimensions of a particle and questions regarding the representativeness of samples, microscopy methods are the best available for particle shape analysis and for characterizing the relationship between particle shape, size, and composition.

2.3.1. Shape Distributions of Size Mode 1

[21] We built particle shape-size distributions from a combination of individual particle (3-D) shapes constructed by *Kalashnikova and Sokolik* [2004] and some new shapes aimed at exploring the effects of particle thickness. Most of the shapes are angular and sharp-edged, as was suggested by our previous work [*Kalashnikova and Sokolik*, 2002]. Random1, random2, and random3 shapes represent particles commonly found in IPA images (Figure 1). Random4-plate, random5-plate, and random6-plate (Figure 2) match reported values of circularity and particle thickness [*Huebert et al.*, 2000; *Okada et al.*, 2001]. Random4-grain, random5-grain and random6-grain (Figure 3) have the same circularity as the corresponding plate-like particle models, but with 3 times larger thickness.

[22] To help describe the 3-D properties of particle shapes, we define particle nonsphericity (NS), the ratio of

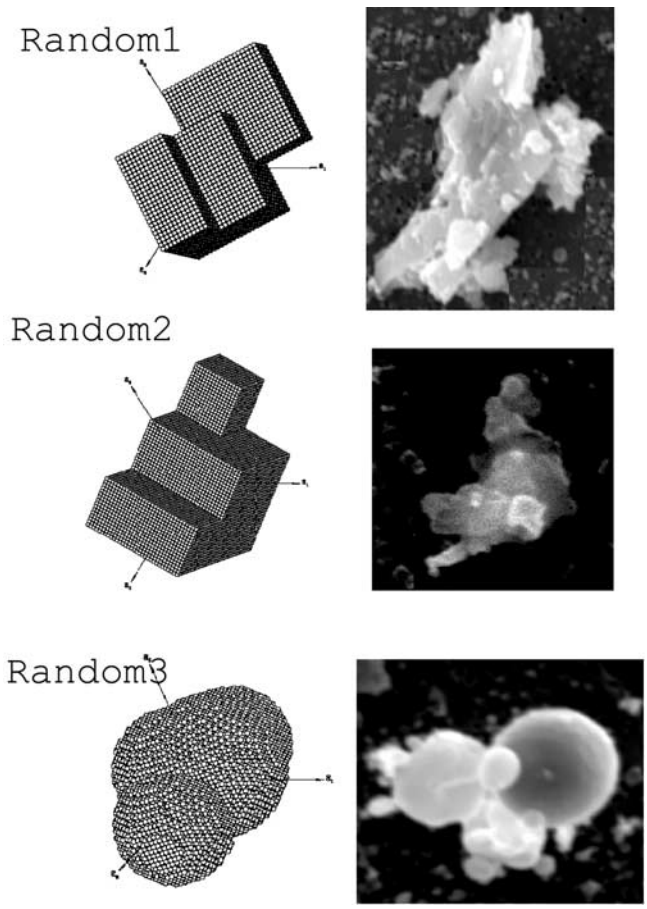

Figure 1. Individual particle irregular shapes used to reconstruct dust shape distributions. Shapes random1–random3 represent shapes in the adjacent SEM images.

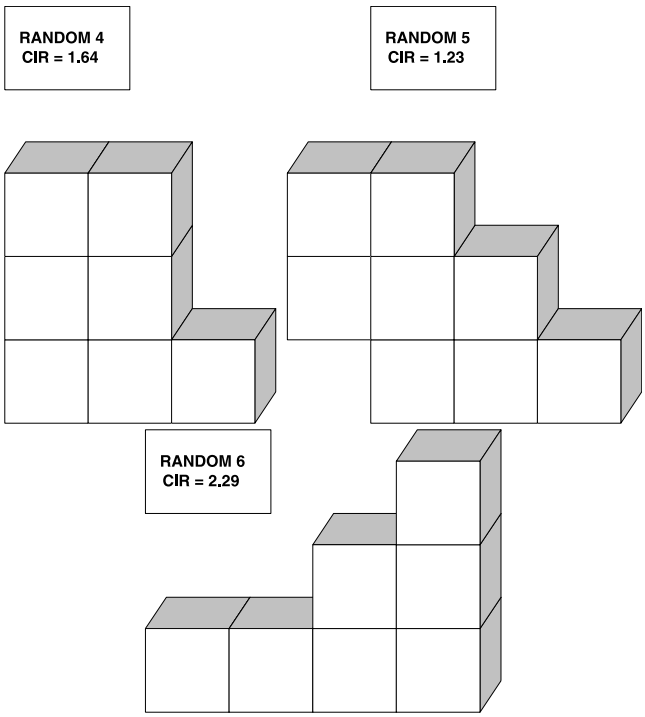

Figure 2. Individual particle irregular shapes used to reconstruct dust shape distributions. Random4-plate to random6-plate reproduce the reported CIR of plate-like particles [*Gao and Anderson*, 2001; *Okada et al.*, 2001].

Table 2. Summary of Geometrical Properties of Representative Particle Shapes

Shape	CIR	NS	h/b	AR(3-D)	Description
Sphere	1.0	1.0	1.	1.	spherical target
Hexagon-plate	1.12	1.342	0.3	3.33	hexagonal plate
Random1-grain	1.61	1.309	1.	1.64	irregular grain
Random2-grain	1.42	1.212	1.	1.50	irregular grain
Random3-grain	1.38	1.173	1.	1.40	smooth irregular
Random4-plate	1.64	1.469	0.3	4.32	irregular plate
Random5-plate	1.93	1.551	0.3	4.68	irregular plate
Random6-plate	2.29	1.582	0.3	4.29	irregular plate
Random4-grain	1.64	1.358	1.	1.50	irregular grain
Random5-grain	1.93	1.441	1.	1.50	irregular grain
Random6-grain	2.29	1.521	1.	1.50	irregular grain

a nonspherical particle's area to that of a sphere of equivalent volume:

$$\mathrm{NS} = \frac{\text{Nonspherical particle surface area}}{\text{Spherical particle surface area}} \tag{3}$$

and particle 3-D aspect ratio:

$$\mathrm{AR}(3-\mathrm{D}) = \frac{\text{Longest dimension}}{\text{Shortest dimension}} \tag{4}$$

in 3-D space.

[23] Calculated 2-D and 3-D geometrical properties of our shapes are listed in Table 2. Note that AR(3-D) is always $\geq h/b$, where h/b is a particle thickness (h is a particle depth and b is a particle width), and that CIR is directly proportional to particle NS if particle thickness is

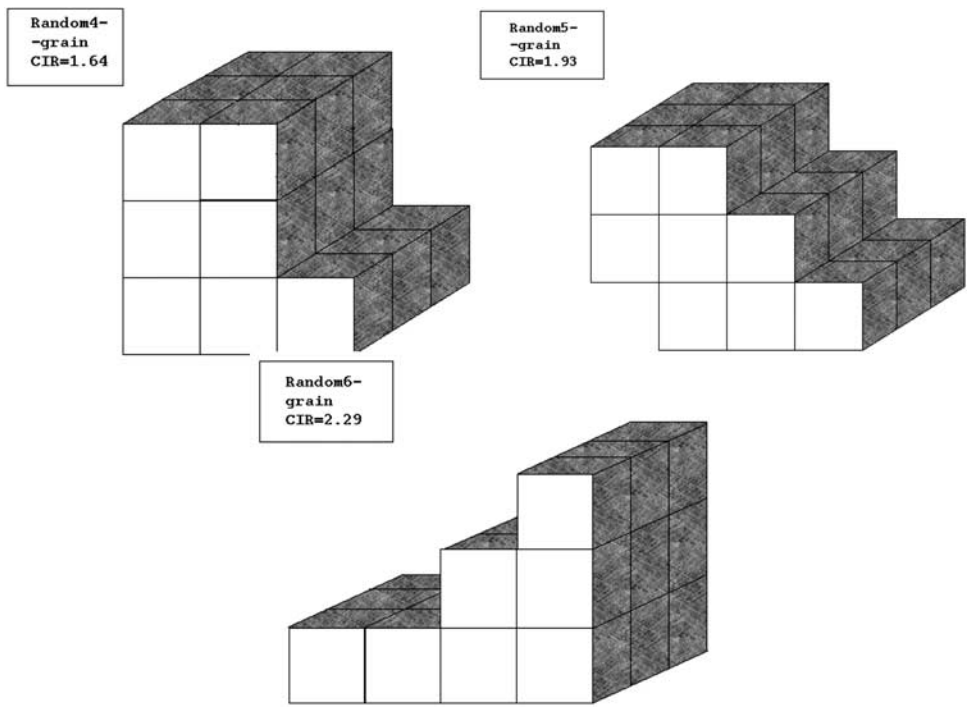

Figure 3. Individual particle irregular shapes used to reconstruct dust shape distributions. Random4-grain to random6-grain reproduce the reported CIR values of grain-like particles [*Gao and Anderson*, 2001; *Okada et al.*, 2001].

fixed. However, for the same CIR, grains have smaller NS than plates and much smaller AR(3-D).

[24] We create shape-size distributions for randomly oriented grains and plates by assigning one shape to each size, in a way that reproduces published relationships between particle circularity and size [*Huebert et al.*, 2000; *Okada et al.*, 2001]. Shape proportions are weighted using the size mode 1 number distribution. We also model a size mode 1 shape distribution that is a mixture of randomly oriented oblate and prolate spheroids [*Mishchenko et al.*, 1997], so we can compare the optical properties of these commonly modeled shapes with more irregular ones.

[25] The shape distributions used in this study are as follows:

[26] 1. Randomly oriented grains (grains) are a shape mixture having CIR linearly increasing with size: [0.10–0.14 μm], spheres; [0.16–0.28 μm], random3-grains; [0.30–0.40 μm], random2-grains; [0.42–0.50 μm], random1-grains; [0.52–0.60 μm], random4-grains; [0.62–0.80 μm], random5-grains; and [0.82–1.00 μm], random6-grains.

[27] 2. Randomly oriented plates (plates) are a mixture of thin particle shapes for which CIR increases linearly with size: [0.1–0.14 μm], spheres; [0.16–0.30 μm], hexagonal plates; [0.32–0.60 μm], random4-plates; [0.62–0.80 μm], random5-plates; [0.82–1.00 μm], random6-plates.

[28] 3. Mixture of randomly oriented oblate and prolate spheroids (O/P spheroids) is a shape mixture having AR(3-D) uniformly distributed between 1.2 and 2.2 [*Mishchenko et al.*, 1997].

[29] Optical properties of size mode 1 randomly oriented grains and plates were calculated using the discrete dipole approximation (DDA) technique, whereas those for the O/P spheroids were calculated using the T matrix technique.

2.3.2. Shape Distribution of Size Mode 2

[30] Practical considerations of computer speed and CPU memory limit the number of dipoles (N_{dip}) that can be treated in a DDA calculation to $N_{dip} < 3 \times 10^6$; this limitation restricts the ratio of particle size to wavelength that can be considered. For the range of wavelengths of interest for this study (0.55–0.85 μm), the largest particle size that meets DDA accuracy criteria has diameter 2 μm (size parameters $2\pi r/\lambda \leq 12$). To calculate optical properties of size mode 2, we use the T matrix algorithm, which is commonly employed to study the optics of nonspherical aerosol particles [*Mishchenko et al.*, 1997] and can calculate the optical properties of particles having large size parameter values, but only for spheroids and other simple shapes. For the large-sized particles included in size mode 2, we can treat only the O/P spheroid shape distribution described for size mode 1.

3. Sensitivity of Modeled Optical Properties to Size Mode 1 and Size Mode 2 Physical Properties

3.1. Modeling Techniques

[31] Because we consider complex composition-shape-size particle mixtures, we need to average dust optical properties weighted over the CSS distribution. We express CSS distributions as a number distribution $N = N_0 \times N(c, s, r)$, where N_0 is the total particle number concentration and $N(c, s, r)$ satisfies the normalization condition:

$$\sum_j \sum_k \sum_l N(c_j, s_k, r_l) = 1 \tag{5}$$

where j, k, and l are index composition, shape, and size, respectively, in a given mixture.

[32] As a first step, the optical properties of each size mode in the bimodal, number-weighted size distribution (equation (2)) were modeled separately and weighted to satisfy (equation (5)). The DDA method was used to model the optical properties of irregular particles in size mode 1, and the T matrix code produced optical properties for ellipsoids in size modes 1 and 2. We calculated volume extinction, scattering, and absorption coefficients, normalized to unit number concentration ($N_0 = 1/\text{cm}^3$), for particle ensembles having specific CSS distributions (*Kalashnikova and Sokolik* [2004]):

$$K^*_{e,s,a} = \sum_j \sum_k \sum_l N(c_j, s_k, r_l) C_{e,s,a}(c_j, s_k, r_l) \tag{6}$$

where C is the per particle coefficient, subscripts e, s, and a are for extinction, scattering, and absorption coefficients, respectively, and parameters c, s, and r indicate the composition, shape, and size distribution models selected. The single scattering albedo is given by

$$\omega_0 = \frac{K^*_s}{K^*_e} \tag{7}$$

[33] The aerosol optical depth of an atmospheric layer containing dust particles with a total particle concentration of N_0 is defined as

$$\tau = N_0 \int_{h1}^{h2} K^*_e dh \tag{8}$$

where h is the vertical path through a layer extending from h_2 to h_2. The asymmetry parameter is defined in the standard way

$$g = \frac{1}{2} \int_{-1}^{1} d\cos(\Theta) P(\Theta) \cos\Theta \tag{9}$$

where $P(\Theta)$ is the scattering phase function and Θ is the scattering angle (angle between the incident and the scattered beam).

[34] The single scattering phase function $P(\Theta)$ was calculated from the first element of the Muller matrix (or phase matrix) as

$$P(\Theta) = \frac{4\pi}{k^2 K^*_s F(\Theta)} \tag{10}$$

where k is the wave factor ($2\pi/\lambda$) and $F(\Theta)$ is the ensemble averaged first element of the Muller matrix [*Mishchenko et al.*, 2000]:

$$F(\Theta) = \sum_j \sum_k \sum_l N(c_j, s_k, r_l) F_{11}(c_j, s_k, r_l) \tag{11}$$

Table 3. Single Scattering Albedos of Four Shape Distributions, at 0.550 μm Wavelength, for Two Composition Types, Averaged Over a Number-Weighted Lognormal Size Distribution With Selected Median Diameters and Standard Deviations

	D_0 = 0.6 μm		D_0 = 1.0 μm	
Shape	σ = 1.5	σ = 2.0	σ = 1.5	σ = 2.0
Composition Type 1, Weakly Absorbing Dust				
Sphere	0.983	0.974	0.970	0.970
Grains	0.984	0.978	0.976	0.974
Plates	0.986	0.982	0.981	0.980
O/P spheroids	0.984	0.975	0.971	0.970
Composition Type 2, Strongly Absorbing Dust				
Sphere	0.842	0.797	0.764	0.763
Grains	0.858	0.816	0.795	0.789
Plates	0.879	0.852	0.838	0.834
O/P spheroids	0.851	0.801	0.770	0.768

The normalization condition for the scattering phase function is

$$\frac{1}{2}\int_0^{\pi} d\Theta P(\Theta)\sin\Theta = 1 \tag{12}$$

[35] To obtain optical properties of the total CSS, the particle number for each size mode was weighted according one of three dust scenarios described in section 2.2, and the total distribution was renormalized to satisfy equation (5). All computations were done with randomly oriented particles and nonpolarized incident light.

[36] The main advantage of the DDA technique, which we use for calculating optical properties of randomly oriented grains and randomly oriented plates in size mode 1, is that it is completely flexible regarding particle shape and composition. With this technique, any particle of complex shape and composition is approximated by an array of dipoles, although a large number of dipoles is required to accurately calculate the optical properties of complex particles. The method gives single scattering albedo with errors less than 1% [*Draine and Flatau*, 1994] if the following criterion is met:

$$|m|kd \le 1 \tag{13}$$

where m is the refractive index, k is the wave factor ($2\pi/\lambda$), and d is the dipole spacing:

$$d = \frac{r_V}{\left(3N_{\text{dip}}/4\pi\right)^{1/3}} \tag{14}$$

Here N_{dip} is the total number of dipoles and r_V is the radius of the volume-equivalent sphere. For scattering phase function computations, the validity criterion is

$$|m|kd \le 0.5 \tag{15}$$

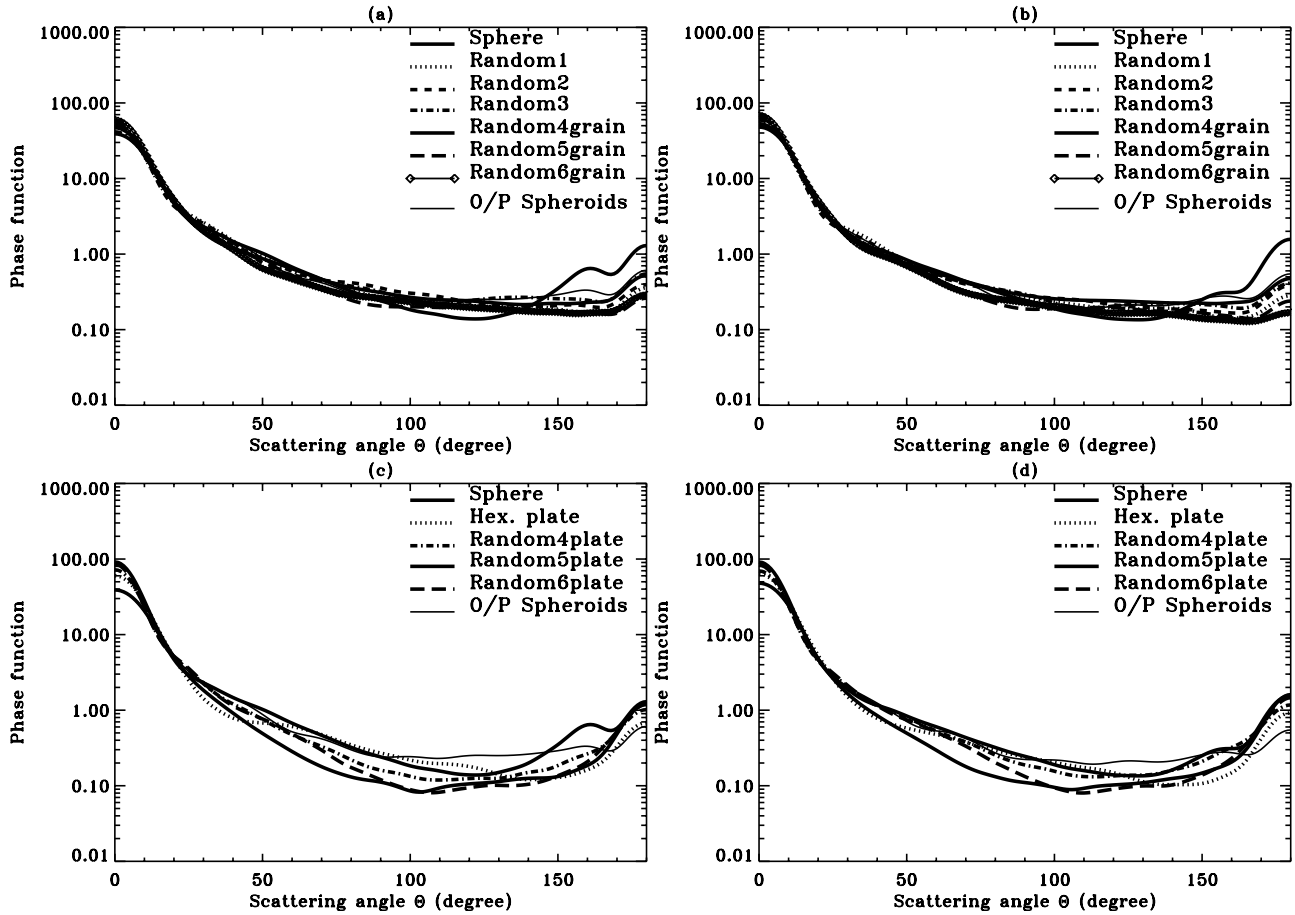

Figure 4. Scattering phase functions of individual (a, b) grain-like shapes and (c, d) plate-like shapes for composition type 1 (Figures 4a and 4c) and 2 (Figures 4b and 4d) at 0.550 μm.

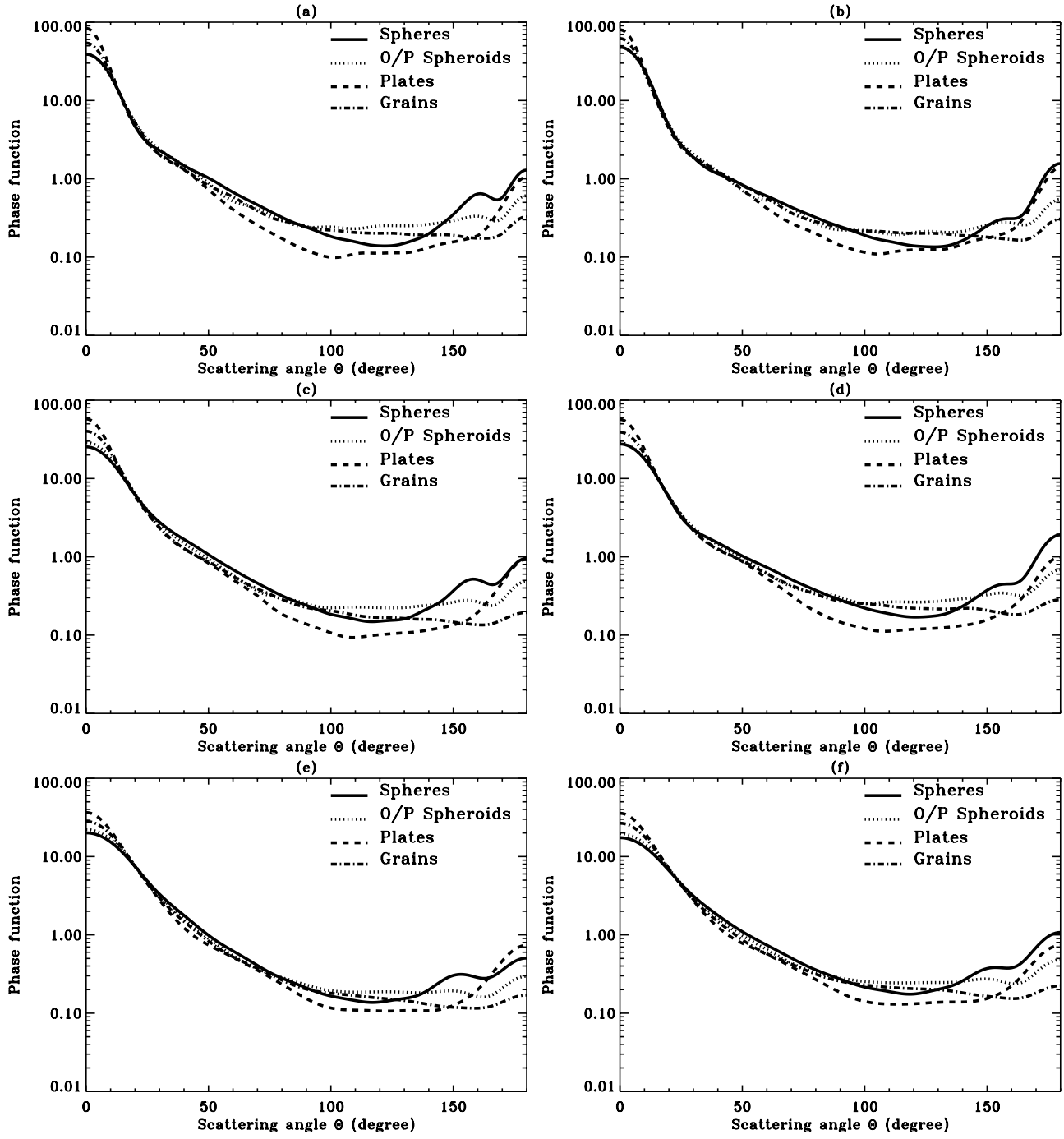

Figure 5. Scattering phase functions of size mode 1 particles with (a, c, e) composition type 1 and (b, d, f) composition type 2 at 0.550 μm (Figures 5a and 5b), 0.672 μm (Figures 5c and 5d) and 0.866 μm (Figures 5e and 5f).

We chose the number of dipoles for each irregular shape to meet this criterion.

[37] The T matrix method, used to calculate optical properties for size mode 2 (diameters up to 12 μm) and ellipsoids for size mode 1, offers relatively fast numerical computations. The disadvantage of essentially all currently available T matrix codes is that they have been customized for computing light scattering by rotationally symmetric nonspherical particles such as spheroids [*Mishchenko et al.*, 1997], finite circular cylinders [*Kuik et al.*, 1994], and Chebyshev particles [*Wiscombe and Mugnai*, 1988]. In our calculations we adopt a mixture of randomly oriented oblate and prolate spheroids [*Mishchenko et al.*, 1997].

[38] In this paper we characterize the size of size mode 1 as the diameter of the equal-volume sphere and of size mode 2 as the diameter of the equal-surface-area sphere. We chose this characterization because a large fraction of size mode 1 particles is significantly smaller than the wavelengths used in this study. Optical properties of this small-sized fraction depend primarily on particle volume rather than on particle

Table 4. Single Scattering Albedo ω_0, Normalized Extinction Coefficient K_e, and Asymmetry Parameter g for Four Shape Distributions[a]

Shape	Weakly Absorbing Dust			Strongly Absorbing Dust		
	ω_0	K_e	g	ω_0	K_e	g
			Channel 0.550 μm			
Spheres	0.9698	2.514	0.661	0.7640	2.423	0.703
Grains	0.9758	3.081	0.673	0.7948	3.023	0.700
Plates	0.9807	3.711	0.788	0.8375	3.566	0.771
O/P spheroids	0.9714	2.662	0.661	0.7705	2.558	0.700
			Channel 0.672 μm			
Spheres	0.988	2.711	0.656	0.926	2.590	0.626
Grains	0.990	3.172	0.693	0.942	3.215	0.654
Plates	0.992	3.744	0.777	0.962	3.802	0.761
O/P spheroids	0.989	2.920	0.674	0.935	2.661	0.630
			Channel 0.866 μm			
Spheres	0.995	3.134	0.695	0.973	2.940	0.627
Grains	0.995	3.334	0.720	0.977	3.323	0.666
Plates	0.995	3.495	0.766	0.980	3.754	0.739
O/P spheroids	0.995	3.251	0.708	0.975	3.132	0.646

[a] K_e in units of 10^{-3} cm^3/km.

surface [*Bohren and Huffman*, 1993]. Thus we compare scattering and absorption properties of spherical and nonspherical particles with the same volume for the smaller-sized particle mode (size mode 1) and with the same average surface area for the larger-sized particle mode (size mode 2). Although this separation prevents us from comparing the effects of large and small modes on forward scattering phase function values directly, we can still compare equivalent particles for each mode.

3.2. Optical Properties of Size Mode 1

3.2.1. Sensitivity of Optical Properties to Particle Size and Composition

[39] To test the sensitivity of size mode 1 optical properties to particle size, we varied the median diameter and the standard deviation in the lognormal size distribution in the range D_0 = 0.6–1.0 μm and σ = 1.5–2.0 μm, respectively, suggested by a variety of experimental measurements [*Reid et al.*, 2003b]. We found that scattering phase functions calculated for three wavelengths and two dust compositions are not sensitive to these size variations at scattering angles larger that 30°. The MISR coverage is normally above 60° scattering angle in midlatitudes, so we do not expect natural size variations for size mode 1 to introduce significant uncertainties in the modeled dust phase functions used in retrievals. The integrated optical properties, especially single scattering albedo, are slightly more sensitive to size mode 1 size variations. As anticipated, when the median diameter and standard deviation decrease, the single scattering albedo increases (Table 3). However, for fixed compositional type, the differences in single scattering albedo due to variations in size parameters are probably not large enough to be detected in MISR retrievals [*Kahn et al.*, 1998]. Therefore we chose a lognormal, number-weighted size distribution with D_0 = 1.0 μm and σ = 1.5 μm as representative distribution of size mode 1.

[40] Size mode 1 optical properties are more sensitive to the range of dust compositional types than to mode 1 size variations adopted in this study. Although the scattering phase functions of the two composition types appear similar, differences in single scattering albedo are significant and could be as large as ~0.21 at 0.550 μm (Table 3). At wavelengths 0.672 and 0.866 μm these compositional differences are smaller but are still of order 0.1. On the basis of previous MISR sensitivity studies [*Kahn et al.*, 1998], we expect MISR to detect differences between weakly and strongly absorbing size mode 1 dust particles.

3.2.2. Sensitivity of Optical Properties to Particle Shape

[41] Before we explore the optical properties of the aggregated shape distributions defined in section 2.3, we consider those of the individual component shapes. Figure 4 shows the scattering phase functions of the individual particles illustrated in Figures 1–3. The single scattering phase functions at 0.550 μm for plate-like and grain-like particles differ noticeably. Compared to volume equivalent spheres, scattering phase functions of thin, irregular plate-like particles, with AR(3-D) > 4, have larger peaks at scattering angles <5°, similar shapes at scattering angles >170°, and flatter behavior in the side scattering directions

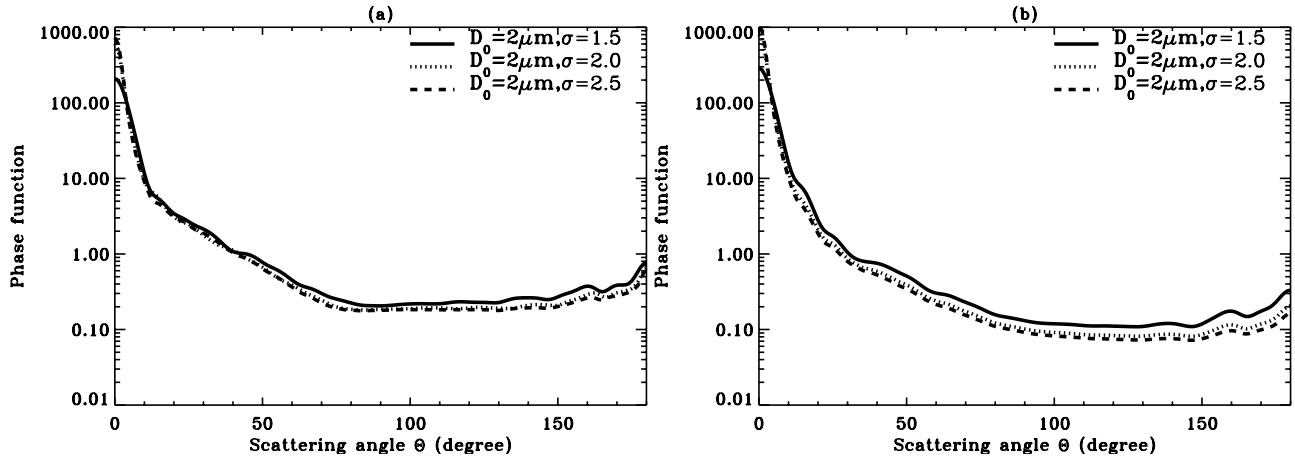

Figure 6. Single scattering phase functions at 0.550 μm for (a) weakly and (b) strongly absorbing size mode 2 O/P spheroids, with median diameter 2 μm and standard deviation in the range 1.5–2.5.

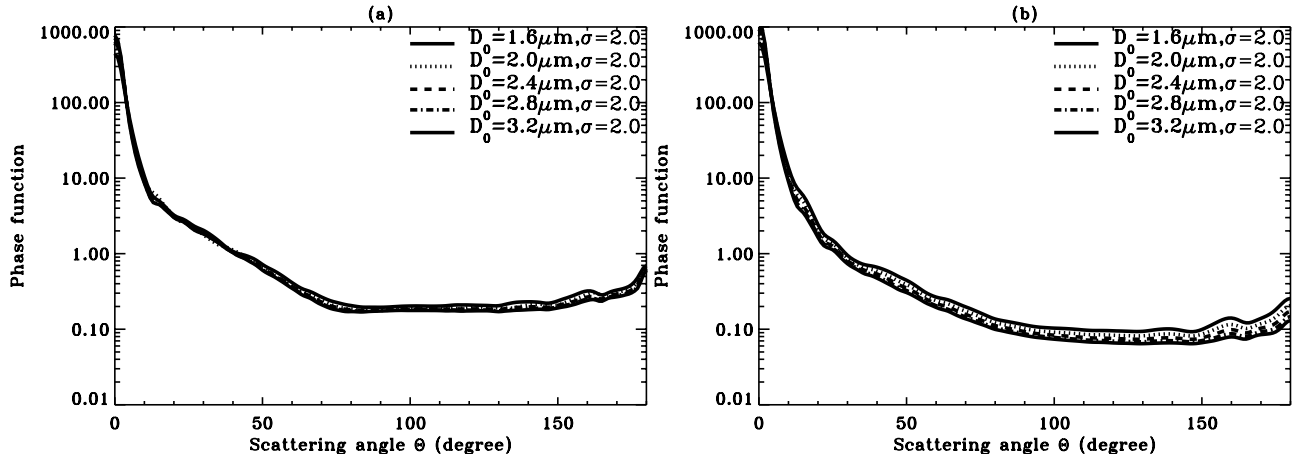

Figure 7. Single scattering phase functions at 0.550 μm for (a) weakly and (b) strongly absorbing size mode 2 O/P spheroids, with median diameter in the range 1.6–3.2 μm and standard deviation 2.0.

(scattering angles from 30° to 160°–170°). Phase functions for equidimensional, irregular, grain-like particles, having AR(3-D) ~1.5, are similar to those of equivalent spheres at scattering angles less than 30°, lower from 30° to 70°, larger from 70° to 140°–150° and much lower for scattering angles >150°. Generally, scattering phase functions for grain-like particles and O/P spheroids are similar in curvature, but have different values at backscattering angles. As CIR and NS increase, the scattering phase functions of all grain-like particles become flatter and lower in the backscattering directions. At 165°, the maximum scattering angle for MISR midlatitude viewing geometry, the random6-grain (CIR = 2.29) scattering phase function is half that of O/P spheroids with identical composition.

[42] These general trends remain after shape-distribution averaging. Figure 5 shows scattering phase functions averaged over grains, plates, and O/P spheroid shape distributions. Figure 5 demonstrates that scattering phase function sensitivity to shape is greatest at backscattering angles ≥145°. We expect these effects to be important for MISR aerosol retrievals.

[43] Table 4 summarizes the integrated optical properties of three complex shape distributions, along with spheres. Plates and grains have larger single scattering albedos than those of spheres and O/P spheroids. However, for the same composition type, the single scattering albedo changes little with shape distribution. The small variation in the single scattering albedo, even as small as 0.1, can have a significant effect to Earth's radiation budget, however it is unlikely to be important for MISR retrievals. The optical effect of shape differences is most pronounced on the scattering phase functions.

3.3. Optical Properties of Size Mode 2

[44] Since size mode 2 is modeled as a mixture of randomly oriented spheroids and *Mishchenko et al.* [1997] extensively studied the effect of assumed shape distribution on optical properties for such particles, we did not need to perform additional sensitivity studies for this attribute. We do adopt the approach of *Mishchenko et al.* [1997] in exploring the sensitivity of size mode 2 optical properties to size and composition.

[45] We vary the size mode 2 median diameter and standard deviation over the range D_0 = 1.6–3.2 μm, and σ = 1.5–2.5 μm, respectively, typical of a mineral dust coarse mode (Figures 6 and 7). Composition type 2, the strongly absorbing particles, varied the most; at 0.550 μm, the single scattering phase function in the scattering angle range [70°–160°], decreases by half when the particle median diameter increases from 1.6 μm to 3.2 μm or when the standard deviation increases from 1.5 to 2.5. For weakly absorbing dust, the scattering phase function changes less than 20%. For the red (0.672 μm) and NIR (0.866 μm) channels used for MISR aerosol retrievals over dark water, size mode 2 single scattering phase functions are affected even less by changes in particle size distribution.

[46] For fixed compositional type, the single scattering albedo also changes little as the size mode 2 distribution varies over the selected parameter space. The largest difference is $\Delta\omega_0$ = 0.08 at 0.550 μm (Table 5), probably not large

Table 5. Size Mode 2 Single Scattering Albedos at 0.550 μm for Ranges of Median Diameter and Standard Deviation

	D_0 = 1.6 μm	D_0 = 2.0 μm	D_0 = 2.4 μm	D_0 = 2.8 μm	D_0 = 3.2 μm
			Weakly Absorbing Dust (Composition Type 1)		
σ = 1.5	0.9411	0.9289	0.9187	0.9098	0.9017
σ = 2.0	0.9091	0.8974	0.8928	0.8872	0.8827
σ = 2.5	0.8928	0.8876	0.8834	0.8801	0.8774
			Strongly Absorbing Dust (Composition Type 2)		
σ = 1.5	0.6850	0.6531	0.6300	0.6142	0.6026
σ = 2.0	0.6277	0.6117	0.6009	0.5933	0.5877
σ = 2.5	0.6009	0.5979	0.5919	0.5875	0.5841

Table 6. Definition of CSS Mixtures With Bimodal Size Distributions

	Size Mode 1		Size Mode 2	
Name	Compositional Type	Shape Distribution	Compositional Type	Shape Distribution
CSS1	1	plates	1	O/P spheroids
CSS2	1	grains	1	O/P spheroids
CSS3	1	O/P spheroids	1	O/P spheroids
CSS4	2	plates	2	O/P spheroids
CSS5	2	grains	2	O/P spheroids
CSS6	2	O/P spheroids	2	O/P spheroids
CSS7	1	plates	2	O/P spheroids
CSS8	1	grains	2	O/P spheroids
CSS9	1	O/P spheroids	2	O/P spheroids
CSS10	2	plates	1	O/P spheroids
CSS11	2	grains	1	O/P spheroids
CSS12	2	O/P spheroids	1	O/P spheroids

enough to affect MISR retrievals, and differences in the red and NIR channels are even smaller. For subsequent sensitivity studies, we therefore choose a lognormal, number-weighted size distribution having $D_0 = 2$ μm and $\sigma = 2$ μm to represent size mode 2 in the red and NIR channel retrievals. If the green channel is used in retrievals, the sensitivity of particle phase function to size distribution will have to be reconsidered.

[47] Differences in single scattering albedo between compositional type 1 and compositional type 2 are on the order of 0.25 (Table 5), large enough to be considered in MISR aerosol retrieval sensitivity studies.

4. CSS Mixtures Averaged Over Bimodal Size Distributions

[48] In this section we investigate properties of scattering phase functions of CSS mixtures averaged over bimodal size distributions. These mixtures are defined in Table 6. These CSS mixtures include cases where particle composition does not change with size (CSS1–CSS3 weakly absorbing cases; CSS4–CSS6 strongly absorbing cases), where particle absorption increases with size (CSS7–CSS9), and where particle absorption decreases with size (CSS9–CSS12).

[49] The relative weights of size modes 1 and 2 are based on the three dust mixing scenarios defined in section 2.1. We expect scenario A might represent dust close to the source, scenario B, dust in the boundary layer [*Clarke et al.*, 2004], and scenario C, high-altitude, long-transported dust.

[50] One of the scattering phase function's distinguishing characteristics is its steepness, which we define as $P11_{max}/P11_{min}$, for specified scattering angle ranges. We consider two ranges: 5° to 173° to compare with measured values reported by *Volten et al.* [2001] and *Muñoz et al.* [2001], and 60° to 165° to investigate CSS phase function curvature in the scattering angle range covered by MISR midlatitude viewing geometry.

[51] Another quantity useful for comparing mixture optical properties is the ratio of the phase function value at the largest scattering angle allowed in the measurements and its minimum value within a range of scattering angles. For the above ranges, we investigated $P11_{173}/P11_{min}$ and $P11_{160}/P11_{min}$, respectively. A third quantity of interest is P(145), the scattering phase function at 145°, a scattering angle at which the phase function may be unaffected by particle nonsphericity [*Kaufman et al.*, 2001].

[52] These quantities are presented in Tables 7–9. We also present phase function attributes of size mode 1 and size mode 2 individually, in Table 10.

[53] The values of steepness and $P11_{160}/P11_{min}$ vary with shape, composition, and size mixing scenario. The effect of particle composition is similar for all three mixing scenarios: steepness and $P11_{160}/P11_{min}$ are lower for CSSs of composition type 1 than for CSSs of composition type 2

Table 7. Phase Function Analysis for Representative CSS Distributions at 0.67 μm for Scenario A (Near-Source Scenario)

Shape	P(145)	P(5)/P(min) [5:173]	P(173)/P(min) [5:173]	P(60)/P(min) [60:165]	P(165)/P(min) [60:165]
CSS1	0.216	463.75	1.894	2.284	1.481
CSS2	0.220	441.69	1.641	2.212	1.369
CSS3	0.227	438.62	1.697	2.195	1.406
CSS4	0.189	643.23	2.263	2.697	1.616
CSS5	0.198	603.01	1.891	2.564	1.460
CSS6	0.204	597.38	1.976	2.518	1.505
CSS7	0.187	651.15	2.255	2.717	1.619
CSS8	0.191	618.36	1.901	2.625	1.471
CSS9	0.200	601.78	1.940	2.547	1.491
CSS10	0.217	461.22	1.909	2.281	1.484
CSS11	0.225	435.86	1.646	2.187	1.370
CSS12	0.231	434.62	1.719	2.168	1.411

Table 8. Phase Function Analysis for Representative CSS Distributions at 0.67 μm for Scenario B (Boundary Layer Scenario)

Shape	P(145)	P(5)/P(min) [5:173]	P(173)/P(min) [5:173]	P(60)/P(min) [60:165]	P(165)/P(min) [60:165]
CSS1	0.205	457.54	2.088	2.424	1.525
CSS2	0.213	420.17	1.577	2.310	1.314
CSS3	0.229	401.87	1.649	2.213	1.353
CSS4	0.182	621.57	2.556	2.889	1.696
CSS5	0.200	542.27	1.779	2.603	1.374
CSS6	0.214	530.59	1.951	2.509	1.465
CSS7	0.178	638.03	2.546	2.936	1.706
CSS8	0.187	571.19	1.795	2.729	1.393
CSS9	0.205	538.93	1.877	2.569	1.436
CSS10	0.209	449.76	2.107	2.404	1.524
CSS11	0.225	404.26	1.574	2.233	1.304
CSS12	0.237	398.04	1.714	2.178	1.381

Table 9. Phase Function Analysis for Representative CSS Distributions at 0.67 μm for Scenario C (Transported Dust Scenario)

Shape	P(145)	P(5)/P(min) [5:173]	P(173)/P(min) [5:173]	P(60)/P(min) [60:165]	P(165)/P(min) [60:165]
CSS1	0.174	466.87	2.958	3.120	1.798
CSS2	0.193	357.74	1.401	2.685	1.161
CSS3	0.234	308.33	1.589	2.384	1.262
CSS4	0.164	554.64	3.504	3.514	1.961
CSS5	0.207	381.88	1.483	2.705	1.150
CSS6	0.243	356.71	1.906	2.515	1.376
CSS7	0.155	597.95	3.547	3.696	2.012
CSS8	0.175	438.39	1.500	3.049	1.179
CSS9	0.220	368.45	1.706	2.627	1.289
CSS10	0.183	441.63	2.967	3.020	1.777
CSS11	0.223	320.78	1.406	2.453	1.147
CSS12	0.256	299.55	1.757	2.297	1.337

Table 10. Phase Function Characteristics for Representative CSS Distributions at 0.67 μm of Size Modes 1 and 2

Shape	Compositional Type	P(145)	P(5)/P(min) [5:173]	P(173)/P(min) [5:173]	P(60)/P(min) [60:165]	P(165)/P(min) [60:165]
			100% of Size Mode 1			
Grains	1	0.155	267.95	1.242	4.390	1.010
Plates	1	0.122	527.02	6.192	5.753	2.862
Grains	2	0.219	191.41	1.298	3.451	1.012
Plates	2	0.138	433.87	5.676	4.994	2.608
O/P spheroids	1	0.246	120.22	1.470	2.739	1.082
O/P spheroids	2	0.302	103.31	1.855	2.543	1.256
			100% of Size Mode 2			
O/P spheroids	1	0.226	477.83	1.761	2.203	1.470
O/P spheroids	2	0.196	662.85	2.001	2.526	1.544

with same shape distributions. It seems likely that this difference can be detected by MISR. However, steepness and $P11_{160}/P11_{min}$ do not show strong differences when absorption increases or decreases with size. The sensitivity of scattering phase function to particle shape is largest for size mode 1 and mixing scenario C (80% of the size mode 1). Plates have significantly larger values of steepness and $P11_{160}/P11_{min}$ than those of O/P spheroids and grains of the same composition. The differences in steepness between O/P spheroids and grains are largest for size mode 1 and mixing scenarios B and C, though they are smaller than those produced by the prescribed compositional changes. P(145) varies with shape distribution, even when composition and size distribution are fixed (Table 10). P(145) for size mode 1, compositional type 1, and grains is almost half that of size mode 1, compositional type 1 O/P spheroids. However, P(145) changes little between O/P spheroids and spheres with the same size and composition. On the basis of these results, if the effect of nonsphericity is ignored at 145° scattering angle, it can introduce significant underestimation of the retrieved optical depth.

[54] *Volten et al.* [2001] measured scattering matrices as functions of scattering angle, in the range 5°–173° at 441.2 and 632.8 nm wavelength, for seven distinct mineral aerosol samples. *Muñoz et al.* [2001] measured scattering matrices for three more samples: fly ash, green clay, and red clay. These data are now available online [*Volten et al.*, 2005]. We expect differences between the measured phase functions and our dust optical models, since the measured samples were collected on the ground, and may not be representative of airborne dust. Because these measurements are limited to scattering angles between 5° and 173°, we renormalize the model CSS phase functions to

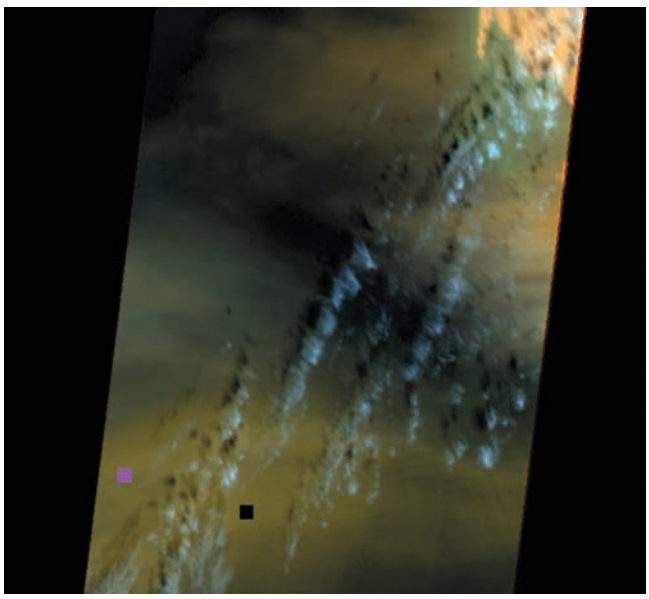

Figure 8. Heavy Saharan dust outbreak over the Cape Verde Islands on 2 March 2003, observed by the MISR 70° forward viewing camera (orbit 17040, path 207, blocks 74–77). The location of the Cape Verde AERONET station is just outside lower left corner; MISR data were analyzed for primary patches, identified by black squares, and secondary patches, indicated by purple squares.

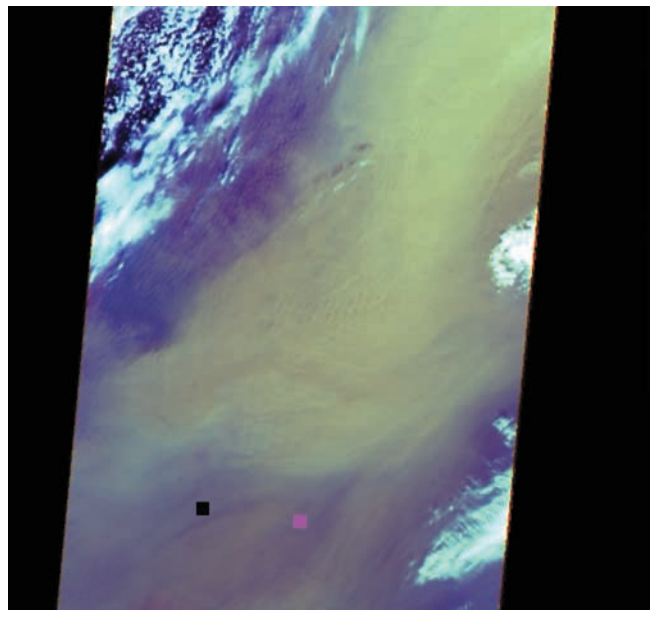

Figure 9. Heavy Asian dust outbreak over the Korean peninsula on 8 April 2002, as observed by the MISR 70° forward viewing camera (orbit 12258, path 119, blocks 57–60). MISR data were analyzed for primary patches, identified by black squares, and secondary patches, indicated by purple squares.

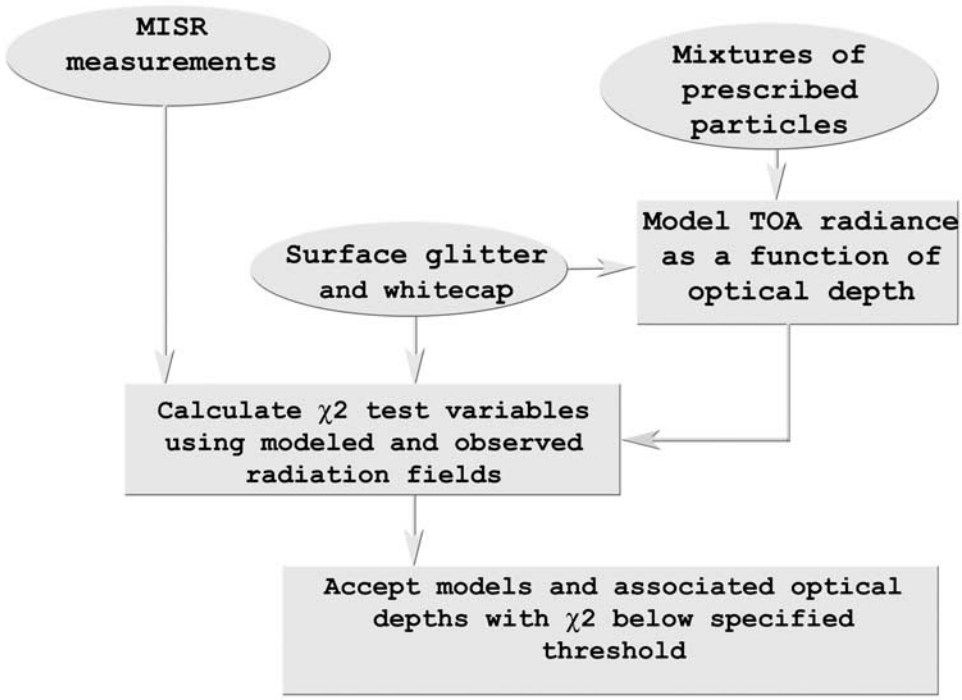

Figure 10. Schematic representation of the MISR aerosol retrieval algorithm over the dark water. Adapted from *Martonchik et al.* [2002].

that angular range when comparing with the measurements. Comparing our calculated values of steepness and $P11_{173}/P11_{min}$ at 0.672 μm to those obtained by *Volten et al.* [2001] and *Muñoz et al.* [2001] at 632.8 nm, we find that the scattering phase functions of size mode 1 grains, compositional types 1 and 2, are very close to those of measured feldspar, green clay, and red clay particles. Since most long-transported, elevated dust particles are aggregated clays [*Sokolik and Toon*, 1999] and layered silicates or feldspar [*Reid et al.*, 2003b], we can expect

Table 11. Phase Function Analysis for Representative CSS at 0.67 μm of Size Modes 1 and 2[a]

Name	Shape	D_{min}	D_{max}	D_0	σ	n_r	n_i
grains_T1_M1	grains	0.20	2.00	1.00	1.50	1.51	0.00110(0.672 μm)
							0.000721(0.866 μm)
grains_T2_M1	grains	0.20	2.00	1.00	1.50	1.60	0.0064(0.672 μm)
						1.59	0.00321(0.866 μm)
plates_T1_M1	plates	0.20	2.00	1.00	1.50	1.51	0.00110(0.672 μm)
							0.000721(0.866 μm)
plates_T2_M1	plates	0.20	2.00	1.00	1.50	1.60	0.0064(0.672 μm)
						1.59	0.00321(0.866 μm)
spheroidal_T1_M1	O/P spheroids	0.20	2.00	1.00	1.50	1.51	0.00110(0.672 μm)
							0.000721(0.866 μm)
spheroidal_T2_M1	O/P spheroids	0.20	2.00	1.00	1.50	1.60	0.0064(0.672 μm)
						1.59	0.00321(0.866 μm)
spheroidal_T1_M2	O/P spheroids	0.20	12.00	2.0	2.0	1.51	0.00110(0.672 μm)
							0.000721(0.866 μm)
spheroidal_T2_M2	O/P spheroids	0.20	12.00	2.0	2.0	1.60	0.0064(0.672 μm)
						1.59	0.00321(0.866 μm)
spherical_T1_M1	sphere	0.20	2.00	1.00	1.50	1.51	0.00110(0.672 μm)
							0.000721(0.866 μm)
spherical_T2_M1	sphere	0.20	2.00	1.00	1.50	1.60	0.0064(0.672 μm)
						1.59	0.00321(0.866 μm)
spherical_T1_M2	sphere	0.20	12.00	2.0	2.0	1.51	0.00110(0.672 μm)
							0.000721(0.866 μm)
spherical_T2_M2	sphere	0.20	12.00	2.0	2.0	1.60	0.0064(0.672 μm)
						1.59	0.00321(0.866 μm)
thin_cirrus (hexagonal_columns)	polyhedral	6.0	400.0	–	–	1.32	1.91×10^{-9}
Sulfate nonabsorbing_0.06	sphere	0.01	0.24	0.06	1.65	1.45	0.00
Sea salt nonabsorbing_1.28	sphere	0.02	20.00	1.28	1.85	1.45	0.00

[a]T1 is compositional type 1 (weakly absorbing) dust, T2 is compositional type 2 (strongly absorbing) dust, M1 is size mode 1, and M2 is size mode 2.

Table 12. Optical Depths, Mixtures, and χ^2 Statistics for the Best Fitting and Next Best Fitting Asian and Saharan Dust Plume Retrievals

	Asian Dust Plume	Saharan Dust Plume
	Best Fitting Mixtures	
τ_{MISR}	2.8	2.3
$\tau_{AERONET}$	–	2.2
Dust, mode 1	70% grains_T1_M1	75% grains_T1_M1
Dust, mode 2	25% spheroidal_T1_M2	15% spheroidal_T1_M2
Sulfate	5%	5%
Sea salt	–	5%
χ^2_{abs}	1.079	0.535
χ^2_{geom}	0.899	0.380
χ^2_{spec}	0.725	0.507
χ^2_{maxdiv}	3.339	1.656
	Next Best Fitting Mixtures	
τ_{MISR}	2.4	1.8
Dust, mode 1	45% grains_T1_M1	80% grains_T1_M1
Dust, mode 2	20% spheroidal_T1_M2	15% spheroidal_T1_M2
Sulfate	35%	5%

size mode 1 grains of compositional types 1 or 2 to be good optical models for transported dust. We examine this possibility in section 5.

5. MISR Retrievals for Optically Thick Dust Plumes Over Dark Water

[55] Having developed a range of CSS models based on particle microphysical properties reported in the literature, we now test the performance of these models in the MISR dark water retrieval for two relatively simple cases: optically thick dust plumes over ocean. We chose optically thick dust plumes to reduce the surface interference and an effect of other aerosols species on the measured radiancies.

[56] The cases were chosen from dust events posted on the Natural Hazards Website in Dust and Smoke Archive (http://earthobservatory.nasa.gov/NaturalHazards/Archive/natural_hazards_archive.php3?topic=dust). One is a Saharan dust plume over the Cape Verde islands on 2 March 2003 and the other is Asian dust over the Korean peninsula on 8 April 2002 (Figures 8 and 9, respectively). MISR data were extracted for three-by-three patches of 1.1 km pixels. The homogeneity of the selected patch is characterized by reflectance variance [*Kahn et al.*, 2001b]. The primary patches were selected to be uniformly homogeneous so the maximum reflectance variance, in all 36 MISR channels, did not exceed 0.5%; for the secondary patches, the reflectances were lower, and the variance did not exceed 0.7%. The dust optical depth during the Cape Verde dust storm was measured, almost simultaneously, by the Cape Verde AERONET Sun photometer; we do not have any optical depth constraints on the Asian dust plume.

[57] We use the MISR research aerosol retrieval (Figure 10) to compare MISR measurements with modeled radiances [*Kahn et al.*, 2001a]. Over ocean, data from up to nine angles, at each of 0.672 and 0.866 μm wavelength, are included. The algorithm creates mixtures of four component particle types, whose optical properties are specified. For each mixture, it calculates top-of-atmosphere reflectances, and compares them with MISR observations using four chi-square test variables [*Kahn et al.*, 1998]:

[58] 1. The variable χ^2_{abs} compares absolute reflectances, and depends primarily on aerosol optical depth for bright aerosols over dark ocean

[59] 2. The variable χ^2_{geom} compares reflectance ratios, normalized to one view angle, and depends mainly on particle size and shape

[60] 3. The variable χ^2_{spec} compares reflectance ratios, normalized to one wavelength, and emphasizes spectral properties

[61] 4. The variable χ^2_{maxdev} selects the single largest term contributing to χ^2_{abs}

[62] Each test variable is normalized to the number of channels used, so a value less than about unity implies that the comparison model is indistinguishable from the measurements. Values larger than a few indicate that the comparison model is unlikely to match the observations.

[63] The maritime cases analyzed in this section may contain sea salt, sulfate particles, or subvisible cirrus, so in addition to two dust modes, we include these as possible third and fourth components in the mixtures considered (Table 11). For the primary patches (Figures 8 and 9), the MISR algorithm found reasonable CSS model solutions for both plumes.

[64] The best fitting mixtures in both cases contain primarily weakly absorbing, size mode 1 grains, along with small fractions of weakly absorbing, size mode 2 O/P spheroids, and background spherical, nonabsorbing particles. Retrieved optical depths and χ^2 statistics for the best candidate models are summarized in Table 12.

[65] The research retrieval algorithm, which was used in our study, reports percentages of the each best fitted candidate model in the modeled radiancies. The standard product of MISR operational retrieval is the contribution to the optical depth of the each best fitted model. Currently, MISR operational retrieval is in the process of incorporating dust models presented in this study. In our future work we plan to use MISR operational product to study contribution to the optical depth of the two size dust modes to determine significance of potential uncertainties in the results due to modeling the larger mode as spheroidal particles.

[66] The best fitting mixture for the Asian dust plume contains 70% size mode 1 dust (composition type 1 grains) + 25% size mode 2 dust (composition type 1 spheroids) + 5% small, nonabsorbing spheres (a sulfate background aerosol model). The best fitting mixture for the Saharan dust plume contains 75% size mode 1 dust (composition type 1 grains) + 15% size mode 2 (composition type 1 spheroids) + 5% small nonabsorbing spheres + 5% medium nonabsorbing spheres (a sea-salt aerosol analog). Values of the next best fitting models are also given in Table 12.

[67] The χ^2 values for mixtures containing composition type 2 dust were greater than 5 for both plumes. So 10% hematite produced too much absorption to match the MISR observations, though iron oxide in intermediate proportions remains to be tested. The χ^2 values for mixtures containing plate dust models, rather than grains, were also too high: greater than 7 for compositional type 1 and over 12 for compositional type 2.

[68] The next best fitting models are similar in composition and size distribution to the best fitting ones, but contain spheroids rather than grains for the dust component. The retrieved optical depths are 20 to 25% lower (Table 12), in

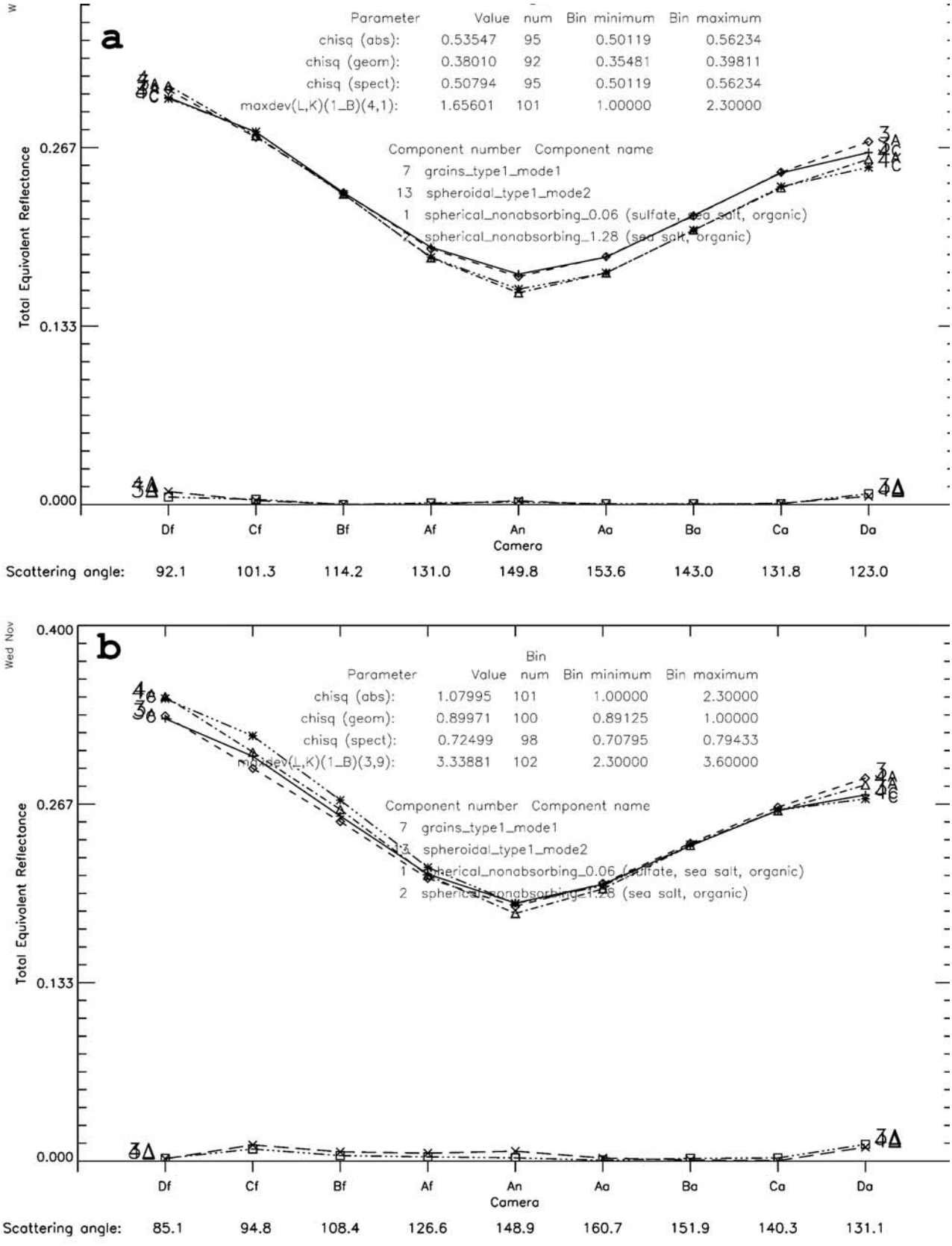

Figure 11. Best fitting model reflectances for the (a) Cape Verde and (b) Korean dust plumes, are plotted as dashed lines for each MISR view, in both the 672 and 867 nm channels (bands 3 and 4, respectively), along with the MISR-observed values (solid lines), and the channel-by-channel differences (dashed lines near the bottom of each plot).

poorer agreement with the AERONET optical depth of 2.2 at 670 nm wavelength, retrieved for Cape Verde on 2 March. These results highlight the importance of modeling shape, and demonstrate that MISR can make the key distinctions, at least in some cases.

[69] A closer look at how the dust models perform in each MISR channel is given by Figure 11. Here the best fitting model reflectances are plotted for each MISR view, in both the 672 and 867 nm channels (bands 3 and 4, respectively), along with the MISR-observed values, and the channel-by-channel differences. In general, the fit is very good at both wavelengths, though the differences increase for the steepest-viewing (Df and Da) cameras. The particle single scattering phase functions are smooth throughout the relevant scattering angle range, and the single-scattering components contribute less than 15% to the model reflectances at these view angles, closer to 20% in the nadir (An) view. The small but increased discrepancies for the steepest-viewing cameras are probably due to model errors, amplified by the cumulative effects of multiple scattering.

[70] We repeated the retrieval analysis for the secondary patches in Figures 8 and 9, and obtained similar results. Again mixtures of size mode 1, composition 1 dust grains dominated the preferred solutions, along with smaller fractions of size mode 2, composition 1 dust spheroids. However, for several patches, the retrieval produced similar χ^2 values when the cirrus model was substituted for dust grains. MISR sensitivity to the differences between these two large, nonspherical particle types is the subject of continuing investigation.

6. Conclusions

[71] The systematic theoretical study of atmospheric mineral dust radiative properties that accounts for recent field and laboratory data on mineral dust morphology and mineralogy including those from the PRIDE and ACE-Asia field campaigns, allow us to develop new optical models for mineral dust, to be used in multiangle satellite aerosol retrieval algorithms. We used DDA and T matrix codes to generate optical models for composition-size-shape distributions covering a range of naturally occurring dust particle properties, and identified the distinguishing characteristics of their single-scattering optical properties.

[72] We tested these models using MISR data for optically thick Saharan and Asian dust plumes that were chosen from dust events posted on the Natural Hazards Website in the Dust and Smoke Archive. Medium-sized, weakly absorbing grains (size mode 1, composition type 1), mixed with smaller fractions of larger-sized, weakly absorbing O/P spheroids (size mode 2, composition type 1) and spherical, nonabsorbing background Maritime particles, gave the best fits to the observations in both cases. Strongly absorbing or plate-like dust particles were rejected by the analysis, though in a few cases, a cirrus optical model gave reasonable solutions as well. The preferred dust models have single scattering phase functions similar to those of the feldspar and clay minerals measured by *Volten et al.* [2001] and *Muñoz et al.* [2001].

[73] Detailed sensitivity studies, using the dust models developed here, along with coincident MISR and field observations taken during the PRIDE and ACE-Asia campaigns, will be presented in the sequel to this work. These future sensitivity studies will address the question why strongly absorbing or plate-like dust particles were rejected by the MISR retrievals. On the basis of recent results of the PRIDE and ACE-Asia field campaigns, we can expect that low-absorbing grain-like aggregated particles are better representative for majority of atmospheric dust particles.

[74] **Acknowledgments.** We thank A. Clarke and J. Reid for providing material in advance of publication and the MISR team for offering facilities, access to data, and useful discussions. The work of O. V. Kalashnikova is supported by a National Research Council postdoctoral fellowship at the Jet Propulsion Laboratory. R. Kahn and W.-H. Li are supported in part by the NASA Earth Sciences Division, Climate and Radiation program, under D. Anderson, and in part by the NASA Earth Observing System Multiangle Imaging Spectroradiometer project, D. J. Diner, Principal Investigator. This work was performed at the Jet Propulsion Laboratory, California Institute of Technology, under contract with NASA. The MISR data were obtained from the NASA Langley Research Center Atmospheric Sciences Data Center.

References

Anderson, J. R. (2003), Variability of dust particle shapes and aggregation in Asian, North African, and North American aerosols, paper presented at 2nd Workshop on Mineral Dust: Physical and Chemical Properties of Dust Particles, Lab. Inter-Univ. des Syst. Atmos., Paris, France.

Anderson, J. R., P. R. Busek, and T. L. Patterson (1992), Characterization of individual fine-fraction particles from the Arctic Aerosol at Spitsbergen, May–June 1987, *Atmos. Environ., Part A*, *26*, 1747–1762.

Bohren, C. F., and D. R. Huffman (1993), *Absorption and Scattering of Light by Nonspherical Particles*, John Wiley.

Choi, J. C., M. Lee, Y. Chun, J. Kim, and S. Oh (2001), Chemical composition and source signature of spring aerosol in Seoul, Korea, *J. Geophys. Res.*, *106*, 18,067–18,071.

Clarke, A. D., et al. (2004), Size distributions and mixtures of dust and black carbon aerosol in Asian outflow: Physiochemistry and optical properties, *J. Geophys. Res.*, *109*, D15S09, doi:10.1029/2003JD004378.

Deuze, J. P., P. Goloub, M. Herman, A. Marchand, G. Perry, S. Susana, and D. Tantre (2000), Estimate of the aerosol properties over the ocean with POLDER, *J. Geophys. Res.*, *105*, 15,329–15,346.

Diner, D. J., G. Asner, R. Davies, Y. Knyazikhin, J. Muller, A. Nolin, B. Pinty, C. Schaaf, and J. Stroeve (1999), New directions in Earth observing: Scientific applications of multiangle remote sensing, *Bull. Am. Meteorol. Soc.*, *80*, 2209–2228.

Draine, B. T., and J. P. Flatau (1994), Discrete-dipole approximation for scattering calculations, *J. Opt. Soc. Am. A Opt. Image Sci.*, *11*, 1491–1499.

Falkovich, A. H., E. Ganor, Z. Levin, P. Formenti, and Y. Rudich (2001), Chemical and mineralogical analysis of individual mineral dust particles, *J. Geophys. Res.*, *106*, 18,029–18,036.

Ganor, E., and Z. Levin (1998), Composition of individual aerosol particles above the Israelian Mediterranean coast during the summer time, *Atmos. Environ.*, *32*, 1631–1642.

Gao, Y., and J. R. Anderson (2001), Characteristics of Chinese aerosols determined by individual particle analysis, *J. Geophys. Res.*, *106*, 18,037–18,045.

Gomes, L., G. Bergametti, G. Coud-Gaussen, and P. Rognon (1990), Submicron desert dusts: A sandblasting process, *J. Geophys. Res.*, *95*, 13,927–13,935.

Huebert, B., et al. (2000), Passing efficiency of a low turbulence inlet: Final report to NSF, technical report, Univ. of Hawaii, Honolulu.

Kahn, R., R. West, D. McDonald, B. Rheingans, and M. Mishchenko (1997), Sensitivity of multiangle remote sensing observations to aerosol sphericity, *J. Geophys. Res.*, *102*, 16,861–16,870.

Kahn, R., P. Banerjee, D. McDonald, and D. Diner (1998), Sensitivity of multiangle imaging to aerosol optical depth and a pure particle size distribution and composition over ocean, *J. Geophys. Res.*, *103*, 32,195–32,213.

Kahn, R., P. Banerjee, and D. McDonald (2001a), The sensitivity of multiangle imaging to natural mixtures of aerosols over ocean, *J. Geophys. Res.*, *106*, 18,219–18,238.

Kahn, R., P. Banerjee, D. McDonald, and J. Martonchik (2001b), Aerosol properties derived from aircraft multiangle imaging over Monterey Bay, *J. Geophys. Res.*, *106*, 11,977–11,995.

Kalashnikova, O. V., and I. N. Sokolik (2002), Importance of shapes and compositions of wind-blown dust particles for remote sensing at solar wavelengths, *Geophys. Res. Lett.*, *29*(10), 1398, doi:10.1029/2002GL014947.

Kalashnikova, O. V., and I. N. Sokolik (2004), Modeling the radiative properties of nonspherical soil-derived mineral aerosols, *J. Quant. Spectrosc. Radiat. Transfer*, *87*(2), 137–166.

Kaufman, Y. J., D. Tanre, O. Dubovik, A. Karnieli, and L. A. Remer (2001), Absorption of sunlight by dust as inferred from satellite and ground-based remote sensing, *Geophys. Res. Lett.*, *28*, 1479–1483.

Koren, I., E. Ganor, and J. H. Joseph (2001), On the relation between size and shape of desert dust aerosol, *J. Geophys. Res.*, *106*, 18,047–18,054.

Kuik, F., J. F. deHaan, and J. W. Hovenier (1994), Single scattering of light by circular cylinders, *Appl. Opt.*, *33*, 4906–4918.

Maring, H., D. L. Savoie, M. A. Izaguirre, L. Custals, and J. S. Reid (2003), Mineral dust aerosol size distribution change during atmospheric transport, *J. Geophys. Res.*, *108*(D19), 8592, doi:10.1029/2002JD002536.

Martonchik, J., D. Diner, K. Crean, and M. Bull (2002), Regional aerosol retrieval results from MISR, *IEEE Trans. Geosci. Remote Sens.*, *40*, 1520–1531.

McLaren, A. C. (1991), *Transmission Electron Microscopy of Minerals and Rocks*, Cambridge Univ. Press, New York.

Mishchenko, M. I., A. A. Lacis, B. E. Carlson, and L. D. Travis (1995), Nonsphericity of dust-like tropospheric aerosols: Implication for aerosol remote sensing and climate modeling, *Geophys. Res. Lett.*, *22*, 1077–1080.

Mishchenko, M. I., L. D. Travis, R. A. Kahn, and R. L. West (1997), Modeling phase functions for dustlike tropospheric aerosols using a shape mixture of polydisperse randomly oriented spheroids, *J. Geophys. Res.*, *102*, 16,831–16,847.

Mishchenko, M. I., J. Hovenier, and L. Travis (2000), *Light Scattering by Nonspherical Particles: Theory, Measurements and Applications*, Springer, New York.

Mishchenko, M. I., I. V. Geogdzhayev, L. Liu, J. A. Ogren, A. A. Lacis, W. B. Rossow, J. W. Hovenier, H. Volten, and O. Munoz (2003), Aerosol retrievals from AVHRR radiances: Effects of particle nonsphericity and absorption and an updated long-term global climatology of aerosol properties, *J. Quant. Spectrosc. Radiat. Transfer*, *79/80*, 953–972.

Muñoz, O., H. Volten, J. de Haan, W. Vassen, and J. Hovenier (2001), Experimental determination of scattering matrices of randomly oriented fly ash at 442 and 633 nm, *J. Geophys. Res.*, *106*, 22,833–22,845.

Okada, K., J. Heintzenberg, K. Kai, and Y. Qin (2001), Shape of atmospheric mineral particles collected in three Chinese arid-regions, *Geophys. Res. Lett.*, *28*, 3123–3126.

Parungo, F., et al. (1995), Asian dust storms and their effects on radiation and climate: part 4, technical report, NOAA Air Resour. Lab., Sci. and Technol. Corp., Hampton, Va.

Prospero, J. M. (1999), Long-range transport of mineral dust in the global atmosphere: Impact of African dust on environment of the southwestern United States, in *Geology, Mineralogy and Human Welfare*, pp. 3396–3403, Natl. Acad. of Sci., Washington, D. C.

Reid, E. A., J. S. Reid, M. M. Meier, M. R. Dunlap, S. S. Cliff, A. Broumas, K. Perry, and H. Maring (2003a), Characterization of African dust transported to Puerto Rico by individual particle and size segregated bulk analysis, *J. Geophys. Res.*, *108*(D19), 8591, doi:10.1029/2002JD002935.

Reid, J. S., et al. (2003b), Comparison of size and morphological measurements of coarse mode dust particles from Africa, *J. Geophys. Res.*, *108*(D19), 8593, doi:10.1029/2002JD002485.

Sokolik, I. N., and O. B. Toon (1999), Incorporation of mineralogical composition into models of the radiative properties of mineral aerosol from UV to IR wavelengths, *J. Geophys. Res.*, *104*, 9423–9444.

Sokolik, I. N., D. Winker, G. Bergametti, D. Gillette, G. Carmichael, Y. Kaufman, L. Gomes, L. Schuetz, and J. Penner (2001), Introduction to special section on mineral dust: Outstanding problems in quantifying the radiative impact of mineral dust, *J. Geophys. Res.*, *106*, 18,015–18,027.

Sviridenkov, A. M., et al. (1993), Size distribution of dust aerosol measured during the Soviet-American experiment in Tadzhikistan 1989, *Atmos. Environ., Part A*, *27*, 2481–2486.

Volten, H., O. Muñoz, E. Rol, J. de Haan, W. Vassen, and J. Hovenier (2001), Laboratory measurements of mineral dust scattering phase function and linear polarization, *J. Geophys. Res.*, *106*, 17,375–17,401.

Volten, H., O. Muñoz, J. W. Hovenier, J. F. de Haan, W. Vassen, W. J. van der Zande, and L. B. F. M. Waters (2005), WWW scattering matrix database for small mineral particles at 441.6 and 632.8 nm, *J. Quant. Spectrosc. Radiat. Transfer*, *90*(2), 191–206.

Wang, J., et al. (2002), Clear-column radiative closure during ACE-Asia: Comparison of multiwavelength extinction derived from particle size and composition with results from Sun photometry, *J. Geophys. Res.*, *107*(D23), 4688, doi:10.1029/2002JD002465.

Wiscombe, W. J., and A. Mugnai (1988), Scattering from nonspherical Chebishev particles, 2, Means of angular scattering patterns, *Appl. Opt.*, *27*, 2405–2421.

R. Kahn, O. V. Kalashnikova, and W.-H. Li, Jet Propulsion Laboratory, MS 169-237, 4800 Oak Grove Dr., Pasadena, CA 91109, USA. (olga.v.kalashnikova@jpl.nasa.gov)

I. N. Sokolik, School of Earth and Atmospheric Sciences, Georgia Institute of Technology, Atlanta, GA 30332-0340, USA.